

## Efficient Vortex Generation in Subwavelength Epsilon-Near-Zero Slabs

Alessandro Ciattoni,<sup>1</sup> Andrea Marini,<sup>2</sup> and Carlo Rizza<sup>1</sup>

<sup>1</sup>*Consiglio Nazionale delle Ricerche, CNR-SPIN, Via Vetoio 10, 67100 L'Aquila, Italy*

<sup>2</sup>*ICFO-Institut de Ciències Fòniques, The Barcelona Institute of Science and Technology, Barcelona, 08860 Castelldefels, Spain*

(Received 5 October 2016; published 10 March 2017)

We show that a homogeneous and isotropic slab, illuminated by a circularly polarized beam with no topological charge, produces vortices of order 2 in the opposite circularly polarized components of the reflected and transmitted fields, as a consequence of the transverse magnetic and transverse electric asymmetric response of the rotationally invariant system. In addition, in the epsilon-near-zero regime, we find that vortex generation is remarkably efficient in subwavelength thick slabs up to the paraxial regime. This physically stems from the fact that a vacuum paraxial field can excite a nonparaxial field inside an epsilon-near-zero slab since it hosts slowly varying fields over physically large portions of the bulk. Our theoretical predictions indicate that epsilon-near-zero media hold great potential as nanophotonic elements for manipulating the angular momentum of the radiation, since they are available without resorting to complicated micro- or nanofabrication processes and can operate even at very small (ultraviolet) wavelengths.

DOI: [10.1103/PhysRevLett.118.104301](https://doi.org/10.1103/PhysRevLett.118.104301)

Spin-orbit interaction (SOI) of light is a very important research topic since it provides a tool for manipulating the spatial degrees of freedom of the radiation by acting on its circular polarization state [1,2]. A remarkable SOI effect is the generation of optical vortices from circularly polarized beams, a process accompanied by spin to orbital angular momentum conversion. Standard procedures to achieve vortex generation are focusing by high-numerical aperture lenses [3,4], scattering by small particles [4], propagation along the optical axis of a homogeneous uniaxial crystal [5,6], interaction with inhomogeneous anisotropic media [7], and propagation through semiconductor microcavities [8]. Similar SOI effects involving Bessel beams have been considered in uniaxial crystals [9] and at reflection and transmission by a planar interface between two homogeneous media [10]. Optical vortex beams have a lot of potential applications such as trapping of particles [11], propagation through atmospheric turbulence [12] and optical communications [13]. The advent of metamaterials has further increased the SOI research effort [14], mostly in the use of ultrathin metasurfaces for manipulating the angular momentum of light [15,16] and for vortex generation [17,18]. Epsilon-near-zero (ENZ) media are nowadays attracting an increasing research interest due to the very unconventional way they affect the electromagnetic radiation. The effective wavelength in ENZ media is much larger than the vacuum wavelength and this entails a regime quite opposite to geometrical optics where the field is slowly varying over relatively large portions of the bulk. Such a feature has been exploited for squeezing electromagnetic waves at will [19], tailoring the antenna radiation pattern [20], and enhancing the nonlinear response of matter [21–25]. In the context of light SOI, it has recently

been proposed that a thin epsilon-near-zero slab can enhance the spin Hall effect of transmitted light [26].

In this Letter we show that a homogeneous, isotropic and ultrathin (subwavelength thick) slab can support vortex generation. We prove that such a genuine SOI effect is physically due to the mutual difference between the dynamics of transverse magnetic (TM) and transverse electric (TE) fields upon reflection and transmission. As the majority of radiation SOI phenomena, the slab vortex generation is mainly a nonparaxial effect. On the other hand, we prove that slab vortex generation in the ENZ regime is remarkably efficient even for incident paraxial beams in spite of the very small slab thickness. Such phenomenology is unprecedented since, to the best of our knowledge, paraxial vortex generation in homogeneous media (i.e., through lenses and uniaxial crystals) requires samples whose thickness is much larger than wavelength. Here, the crucial role is played by the physical ability of an ENZ slab to turn a paraxial wave, incoming from vacuum, into a nonparaxial one within the bulk, its nonparaxiality triggering the predicted slab vortex generation. The vortex generation method proposed in this Letter can have important nanophotonic applications since, unlike the one based on metasurfaces, it does not require microfabrication (the ENZ slab is homogeneous) and it is scalable down to very small wavelengths (exploiting the ultraviolet ENZ point of metals) where metamaterials are not available. It is also worth noting that our method, unlike the one based on inhomogeneous anisotropic media ( $q$  plates), is based on a very simple setup that requires neither preparation nor external biasing by electric field; it operates in subwavelength thick slabs and it can be used even up to the ultraviolet frequencies.

Let us consider the scattering of a monochromatic [ $\sim \exp(-i\omega t)$ ] electromagnetic field by a homogeneous and isotropic slab of thickness  $L$  and dielectric permittivity  $\varepsilon$  (see Fig. 1). We choose the  $z$  axis to be along the slab normal. The angular spectrum representations of both the incident ( $i$ ) and transmitted ( $t$ ) fields are ( $q = i, t$ )

$$\mathbf{E}^{(q)} = \int d^2\mathbf{k}_\perp e^{i\mathbf{k}_\perp \cdot \mathbf{r}_\perp + ik_z^{(V)}z} [\mathbf{V}_{\text{TM}} U_{\text{TM}}^{(q)} + \mathbf{V}_{\text{TE}} U_{\text{TE}}^{(q)}], \quad (1)$$

where  $\mathbf{r}_\perp = x\hat{\mathbf{e}}_x + y\hat{\mathbf{e}}_y$ , and  $\mathbf{k}_\perp = k_x\hat{\mathbf{e}}_x + k_y\hat{\mathbf{e}}_y$  are the transverse position and wave vector, respectively,  $k_z^{(V)}(k_\perp) = \sqrt{k_0^2 - k_\perp^2}$  is the longitudinal vacuum wave vector ( $k_0 = \omega/c$ ),  $\mathbf{V}_{\text{TM}} = (k_x\hat{\mathbf{e}}_x + k_y\hat{\mathbf{e}}_y/k_\perp) - (k_\perp\hat{\mathbf{e}}_z/k_z^{(V)})$  and  $\mathbf{V}_{\text{TE}} = (-k_y\hat{\mathbf{e}}_x + k_x\hat{\mathbf{e}}_y/k_\perp)$  are the TM and TE polarization vectors, and  $U_{\text{TM}}^{(q)}(\mathbf{k}_\perp)$  and  $U_{\text{TE}}^{(q)}(\mathbf{k}_\perp)$  are their corresponding amplitudes. The slab differently transmits TM and TE fields according to  $U_{\text{TM}}^{(t)} = t_{\text{TM}}(k_\perp)U_{\text{TM}}^{(i)}$  and  $U_{\text{TE}}^{(t)} = t_{\text{TE}}(k_\perp)U_{\text{TE}}^{(i)}$  where the complex transmissivities are  $t_{\text{TM}} = [\cos(k_z^{(S)}L) - \frac{i}{2}[(\varepsilon k_z^{(V)}/k_z^{(S)}) + (k_z^{(S)}/\varepsilon k_z^{(V)})]\sin(k_z^{(S)}L)]^{-1}$  and  $t_{\text{TE}} = [\cos(k_z^{(S)}L) - \frac{i}{2}[(k_z^{(V)}/k_z^{(S)}) + (k_z^{(S)}/k_z^{(V)})]\sin(k_z^{(S)}L)]^{-1}$ , where  $k_z^{(S)}(k_\perp) = \sqrt{k_0^2\varepsilon - k_\perp^2}$  is the longitudinal wave vector inside the slab. We now choose, as a basis for the transverse plane, the LHC and RHC polarization unit vectors,  $\hat{\mathbf{e}}_L = (1/\sqrt{2})(\hat{\mathbf{e}}_x + i\hat{\mathbf{e}}_y)$  and  $\hat{\mathbf{e}}_R = (1/\sqrt{2})(\hat{\mathbf{e}}_x - i\hat{\mathbf{e}}_y)$ , respectively, and we introduce polar coordinates,  $x = r_\perp \cos \varphi$ ,  $y = r_\perp \sin \varphi$ ,  $k_x = k_\perp \cos \theta$ ,  $k_y = k_\perp \sin \theta$ , for both transverse position and wave vector. Accordingly, the transverse component of Eq. (1) becomes

$$\begin{aligned} \mathbf{E}_\perp^{(q)} = & \int_0^{+\infty} dk_\perp k_\perp \int_0^{2\pi} d\theta e^{ik_\perp r_\perp \cos(\theta-\varphi) + ik_z^{(V)}z} \\ & \times \left[ e^{-i\theta} \left( \frac{U_{\text{TM}}^{(q)} - iU_{\text{TE}}^{(q)}}{\sqrt{2}} \right) \hat{\mathbf{e}}_L + e^{i\theta} \left( \frac{U_{\text{TM}}^{(q)} + iU_{\text{TE}}^{(q)}}{\sqrt{2}} \right) \hat{\mathbf{e}}_R \right]. \end{aligned} \quad (2)$$

We consider an incident beam that is LHC polarized (carrying spin angular momentum) and that has no topological charge (i.e., not carrying orbital angular momentum). From Eq. (2), it follows that its TM and TE spectral amplitudes have to satisfy the constraint  $U_{\text{TE}}^{(i)} = iU_{\text{TM}}^{(i)}$  that, together with the zero-topological charge condition, implies that  $U_{\text{TM}}^{(i)} = e^{i\theta}U^{(i)}(k_\perp)$  and  $U_{\text{TE}}^{(i)} = ie^{i\theta}U^{(i)}(k_\perp)$ , where  $U^{(i)}$  is an arbitrary rotationally invariant spectrum. As a matter of fact, Eq. (2) with  $q = i$ , after performing the angular integration, yields

$$\mathbf{E}_\perp^{(i)} = 2\pi \int_0^{+\infty} dk_\perp k_\perp e^{ik_z^{(V)}z} [\sqrt{2}J_0(k_\perp r_\perp)\hat{\mathbf{e}}_L]U^{(i)}, \quad (3)$$

where  $J_n(\xi)$  is the Bessel function of the first kind of order  $n$ . The TM and TE components of the field transmitted by the

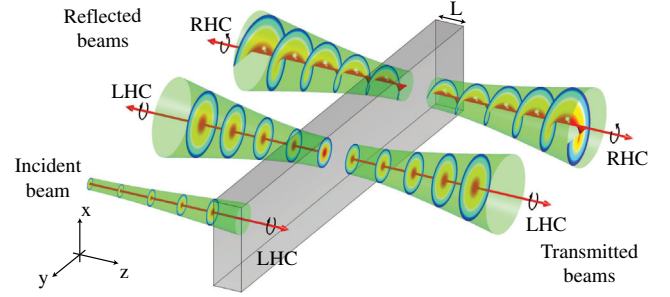


FIG. 1. Geometry of the vortex generation process. The incident beam is left-handed circular (LHC) polarized with no topological charge. Both the reflected and the transmitted beams have a LHC component with no topological charge and a right-handed circular (RHC) component containing a second-order vortex. (The beams in the figure are spatially separated for clarity purposes).

slab are therefore  $U_{\text{TM}}^{(t)} = t_{\text{TM}}e^{i\theta}U^{(i)}$  and  $U_{\text{TE}}^{(t)} = t_{\text{TE}}ie^{i\theta}U^{(i)}$  and accordingly Eq. (2) with  $q = t$ , after performing the angular integration, yields

$$\begin{aligned} \mathbf{E}^{(t)} = & 2\pi \int_0^{+\infty} dk_\perp k_\perp e^{ik_z^{(V)}z} \left[ \left( \frac{t_{\text{TM}} + t_{\text{TE}}}{\sqrt{2}} \right) J_0(k_\perp r_\perp)\hat{\mathbf{e}}_L \right. \\ & \left. - e^{i2\varphi} \left( \frac{t_{\text{TM}} - t_{\text{TE}}}{\sqrt{2}} \right) J_2(k_\perp r_\perp)\hat{\mathbf{e}}_R \right] U^{(i)}. \end{aligned} \quad (4)$$

Equation (4) reveals that the RHC component of the transmitted field, due to the factor  $e^{i2\varphi}$ , contains a second-order vortex (i.e., its topological charge is equal to 2), whereas the LHC component has no topological charge as the incident field. Evidently the reflected beam has the same polarization and vortex structure. The geometry of the incident, reflected, and transmitted fields is sketched in Fig. 1. In addition, Eq. (4) clearly shows that the generation of the transmitted RHC field (containing the vortex) is a consequence of condition  $t_{\text{TM}} \neq t_{\text{TE}}$ , i.e., of the different behavior of TM and TE fields upon slab transmission. Physically this is due to the fact that the TM and TE spectral amplitudes of the incident LHC polarized field are related by the constraint  $U_{\text{TE}}^{(i)} = iU_{\text{TM}}^{(i)}$  that, due to the different slab effect on TM and TE fields, is not transferred to the transmitted field, which accordingly is not LHC polarized. A fundamental role in the considered vortex generation process is played by the factors  $e^{-i\theta}$  and  $e^{i\theta}$  of Eq. (2). As a matter of fact the topological charge factor  $e^{i2\varphi}$  appears (after the integration on  $\theta$ ) since the  $e^{i\theta}$  factor is literally carried from the spectral amplitude of the incident field  $e^{i\theta}U^{(i)}$  to the RHC component of the transmitted one, where it is multiplied by the further polarization factor  $e^{i\theta}$ .

To investigate the vortex generation process in more detail, we consider slabs of permittivity  $\varepsilon = \text{Re } \varepsilon + 0.003i$

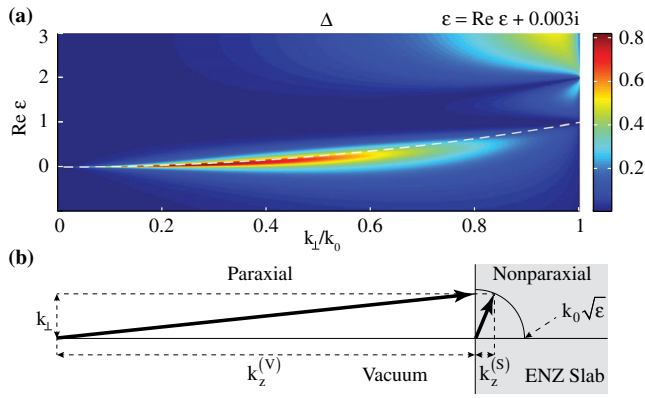


FIG. 2. (a) Vortex spectral amplitude  $\Delta = |t_{\text{TM}} - t_{\text{TE}}|$  versus  $k_{\perp}/k_0$  and  $\text{Re } \epsilon$ . The white dashed line is the curve  $k_{\perp} = k_0\sqrt{\text{Re } \epsilon}$ . (b) Excitation of nonparaxial waves within the ENZ slab by vacuum paraxial waves.

and subwavelength thickness  $L = \frac{1}{2}\lambda$  ( $\lambda = (2\pi c/\omega)$  is the vacuum wavelength) and we focus on the absolute value of the difference between the TM and TE transmissivities,  $\Delta = |t_{\text{TM}} - t_{\text{TE}}|$ . This is the key spectral parameter ruling vortex generation in the transmitted RHC component of Eq. (4). In Fig. 2(a) we plot  $\Delta$  as a function of the real part of the slab permittivity and of the transverse wave vector  $k_{\perp}$  (normalized to the vacuum wave number  $k_0$ ) spanning the vacuum homogeneous spectrum ( $k_{\perp} < k_0$ ). For standard materials,  $\text{Re } \epsilon > 1$ ,  $\Delta$  is rather small except for  $k_{\perp}$  close to  $k_0$ . This is consistent with the general nonparaxial trait of SOI optical effects [2]. For materials characterized by the condition  $|\text{Re } \epsilon| < 1$  the situation is remarkably different in that  $\Delta$  has a marked lobe, localized at the middle of the vacuum homogeneous spectrum, whose left tail encompasses very small transverse wave vectors  $k_{\perp} \ll k_0$  around  $\text{Re } \epsilon = 0$ . This proves that vortex generation in ENZ subwavelength thick slabs can efficiently be observed even in the paraxial regime, the smaller the  $\text{Re } \epsilon$  the more paraxial the field. To physically grasp the mechanism supporting paraxial vortex generation in ENZ slabs, in Fig. 2(a) we have also plotted the curve  $k_{\perp} = k_0\sqrt{\text{Re } \epsilon}$  (white dashed line), which is found to locate the largest values of  $\Delta$  on the lobe. Since  $|k_z^{(S)}| = k_0\{\text{Re } \epsilon - (k_{\perp}^2/k_0^2)\}^{1/4} + (\text{Im } \epsilon)^2\}^{1/4}$ , it is evident that the longitudinal wave vector within the slab attains its minimum absolute value  $|k_z^{(S)}|_{\text{min}} = k_0\sqrt{\text{Im } \epsilon}$  at all points of the curve. Therefore, vortex generation is efficient in the paraxial regime since, if  $0 < \text{Re } \epsilon < 1$ , there is a narrow bundle of vacuum paraxial waves whose  $k_{\perp}$  is smaller than and close to  $k_0\sqrt{\text{Re } \epsilon}$  and they excite highly nonparaxial waves within the slab, their wave vector being almost orthogonal to the  $z$  axis. In Fig. 2(b) we have sketched a wave vector diagram showing the excitation of nonparaxial waves in the ENZ slab by paraxial vacuum waves in the ideal  $\text{Im } \epsilon = 0$  situation. It is evident that the smaller the value  $|k_z^{(S)}|_{\text{min}} = k_0\sqrt{\text{Im } \epsilon}$  the

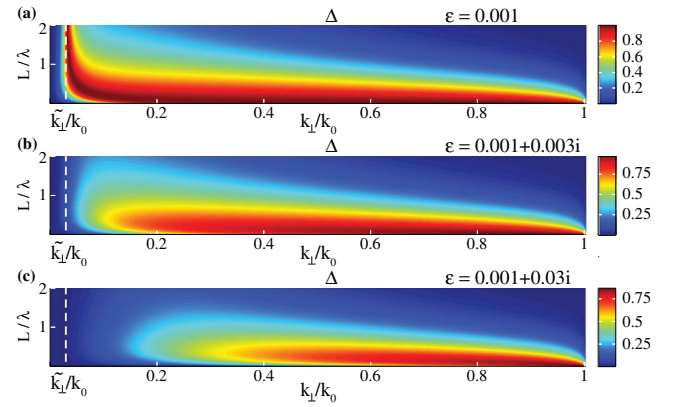


FIG. 3. Vortex spectral amplitude  $\Delta$  versus  $k_{\perp}/k_0$  and  $L/\lambda$ , for (a)  $\epsilon = 0.001$ , (b)  $\epsilon = 0.001 + 0.003i$ , and (c)  $\epsilon = 0.001 + 0.03i$ . The white dashed lines indicate  $\tilde{k}_{\perp} = k_0\sqrt{\text{Re } \epsilon} \approx 0.031k_0$

more nonparaxial the waves are within the slab so that the full ENZ condition  $|\epsilon| \ll 1$  has to be met to achieve efficient vortex generation. The imaginary part of  $\epsilon$ , due to the slab losses, also plays an important role as combined to the slab thickness  $L$ . In Fig. 3 we plot the vortex spectral amplitude  $\Delta$  as a function of the slab thickness  $L$  (normalized to the vacuum wavelength  $\lambda$ ) and of the transverse wave vector  $k_{\perp}$  (normalized to the vacuum wave number  $k_0$ ) spanning the vacuum homogeneous spectrum ( $k_{\perp} < k_0$ ), for three different slabs with permittivities (a)  $\epsilon = 0.001$ , (b)  $\epsilon = 0.001 + 0.003i$ , and (c)  $\epsilon = 0.001 + 0.03i$ . In the first (ideal) case paraxial vortex generation around  $\tilde{k}_{\perp} = k_0\sqrt{\text{Re } \epsilon} \approx 0.031k_0$  (labeled with the vertical white dashed line) is persistent even for  $L$  greater than  $\lambda$ . This is due to the fact that in this case, we have  $t_{\text{TM}}(\tilde{k}_{\perp}) = (1 - (i/2)\epsilon\sqrt{1 - \epsilon k_0 L})^{-1}$  and  $t_{\text{TE}}(\tilde{k}_{\perp}) = (1 - (i/2)\sqrt{1 - \epsilon k_0 L})^{-1}$  so that, since  $\epsilon \ll 1$ , the TM transmissivity is slowly varying with  $L$  and very close to 1, whereas the TE transmissivity quickly decreases as  $L$  increases thus producing a large value of  $\Delta$ . In the other two cases [see Figs. 3(b) and 3(c)], the imaginary part is larger and its detrimental effect on vortex generation is evident since  $\Delta$  fades as the slab thickness  $L$  increases. This is a consequence of the fact that absorption in the ENZ regime is generally not negligible even if  $\text{Im } \epsilon$  is rather small. However, if the slab has subwavelength thickness, vortex generation persists even up to the paraxial regime.

In order to discuss the vortex generation process in realistic and feasible situations, we consider subwavelength thick slabs whose dielectric dispersive response is described by the Drude model  $\epsilon = \epsilon_{\infty} - (\omega_p^2/\omega^2 + i\gamma\omega)$ , where  $\epsilon_{\infty}$  is the high-frequency permittivity,  $\gamma$  is the damping rate, and  $\omega_p$  is the free-electron plasma frequency. Such materials have a zero crossing point  $\text{Re } \epsilon = 0$  at the vacuum wavelength  $\lambda_0$ . For simplicity we consider impinging LHC polarized Bessel beams of radius  $w$ , without

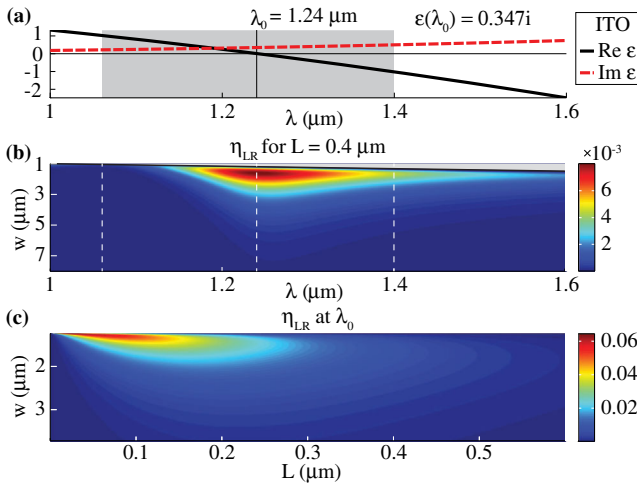


FIG. 4. (a)  $\text{Re } \epsilon$  and  $\text{Im } \epsilon$  of ITO. (b) Vortex generation efficiency  $\eta_{LR}$  for Bessel beams by an ITO slab of thickness  $L = 0.4 \mu\text{m}$  versus  $\lambda = 2\pi c/\omega$  and  $w$ . (c) Vortex generation efficiency  $\eta_{LR}$  at  $\lambda_0$  by ITO slabs versus  $L$  and  $w$ .

topological charge, which are scattered by the slab to produce transmitted RHC Bessel beams of the same radius and carrying topological charge 2. The efficiency of the vortex generation process is  $\eta_{LR} = \frac{1}{4} |t_{\text{TE}}(2\pi/w) - t_{\text{TM}}(2\pi/w)|^2$  (see Supplemental Material [27]).

In the first example we consider an indium tin oxide (ITO) slab of thickness  $L = 0.4 \mu\text{m}$  whose Drude parameters are  $\epsilon_\infty = 3.8055$ ,  $\omega_p = 2.9719 \times 10^{15}$  Hz, and  $\gamma = 0.0468\omega_p$  [24], for which  $\lambda_0 = 1.24 \mu\text{m}$  and  $\text{Im}[\epsilon(\lambda_0)] = 0.347$ . In Fig. 4(a) we plot the real and imaginary parts of ITO permittivity in the infrared spectral band  $1 \mu\text{m} < \lambda < 1.6 \mu\text{m}$  and we have shadowed the spectral region  $|\text{Re } \epsilon| < 1$  where, from the above discussion, vortex generation is expected to occur even in the paraxial regime. In Fig. 4(b) we plot the Bessel vortex generation efficiency  $\eta_{LR}$  as a function of the vacuum wavelength  $\lambda = 2\pi c/\omega$  and the beam width  $w$ . In the nonparaxial regime,  $w \approx \lambda$ ,  $\eta_{LR}$  is sensibly different from 0 at least for wavelengths smaller than  $\lambda_0$ . This is the above-discussed vortex generation for nonparaxial fields occurring in dielectric slabs [since  $\text{Re } \epsilon > 0$  for  $\lambda > \lambda_0$ ; see Fig. 4(a)]. In the paraxial regime  $w > \lambda$ ,  $\eta_{LR}$  is very small except for a region surrounding the wavelength  $\lambda_0$  where  $\eta_{LR}$  fades as  $w$  increases. This shows that vortex generation is effectively operated by the considered ITO slab in the paraxial regime only for wavelength close to the ENZ crossing point. In Fig. 4(c) we plot  $\eta_{LR}$  at  $\lambda_0$  as a function of the slab thickness  $L$  and the beam width  $w$ . Note that the vortex generation efficiency in this example is rather small as a consequence of the large imaginary part of  $\epsilon$  at  $\lambda_0$ , which prevents the full ENZ condition  $|\epsilon| \ll 1$  being fulfilled. In addition, the large slab losses restrict vortex generation to very thin slabs  $L \lesssim 0.3 \mu\text{m} \approx \frac{1}{4}\lambda_0$ . In the second example we consider a Na slab of thickness  $L = 100 \text{ nm}$  whose Drude parameters

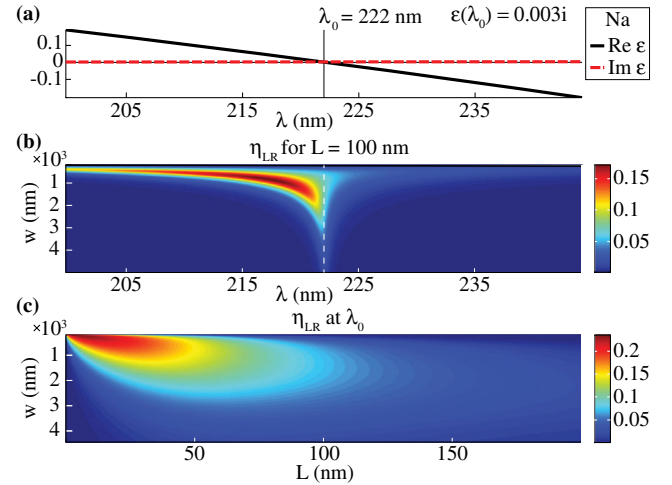


FIG. 5. (a)  $\text{Re } \epsilon$  and  $\text{Im } \epsilon$  of sodium (Na). (b) Vortex generation efficiency  $\eta_{LR}$  for Bessel beams by a Na slab of thickness  $L = 100 \text{ nm}$  versus  $\lambda = 2\pi c/\omega$  and  $w$ . (c) Vortex generation efficiency  $\eta_{LR}$  at  $\lambda_0$  by Na slabs versus  $L$  and  $w$ .

are  $\epsilon_\infty = 1$ ,  $\omega_p = 8.2 \times 10^{15}$  Hz, and  $\gamma = 0.003\omega_p$  [28], for which  $\lambda_0 = 222 \text{ nm}$  and  $\text{Im}[\epsilon(\lambda_0)] = 0.003$ . In Figs. 5(a) and 5(b) we focus on the ultraviolet spectral band  $200 \text{ nm} < \lambda < 245 \text{ nm}$  and, in analogy with Fig. 4, we plot the permittivity and vortex generation efficiency of the considered Na slab. This example shows all the above discussed features of slab vortex generation but its efficiency is larger than in the first example. In Fig. 5(c) we plot  $\eta_{LR}$  at  $\lambda_0$  as a function of the slab thickness  $L$  and the beam width  $w$  and, as compared with Fig. 4(c), it reveals both the larger vortex generation efficiency and the persistence of the phenomenon up to very wide paraxial fields (where  $w \approx 18\lambda_0$  for  $w = 4000 \text{ nm}$ ). This is due to the small imaginary part of  $\epsilon$  at  $\lambda_0$ , which allows the Na slab to host the genuine ENZ regime  $|\epsilon| \ll 1$  close to  $\lambda_0$ . The large impact of losses in the ENZ regime restricts vortex generation to subwavelength slabs of thickness  $L \lesssim 100 \text{ nm} \approx \frac{1}{2}\lambda_0$ . The two considered examples reveal that the proposed vortex generation mechanism can easily be spectrally tuned from infrared to ultraviolet wavelengths. We envisage that such tunability can be extended to the visible range where homogeneous plasmonic materials (e.g., transition metal nitrides such as TiN, ZrN, HfN, etc. [29,30]) having a crossing point of the permittivity at optical frequencies are currently the subject of intense research activity.

In conclusion we have shown that a subwavelength thick slab supports efficient vortex generation of nonparaxial fields. We believe that the identified vortex generation mechanism based on TE/TM asymmetry further increases the understanding of SOI of light. If the slab is in the ENZ regime, its ability to convert spin into angular orbital momentum extends to the paraxial regime. This is a remarkable effect in view of the homogeneity of the slab and its extremely small thickness, which is made possible

by the conversion of a paraxial field into a nonparaxial one operated by the ENZ slab. As compared to standard vortex generation techniques based on metasurfaces, our method is based on a very simple setup, the homogenous ENZ slab, which does not require microfabrication. In addition our scheme can be exploited even for very small ultraviolet wavelengths where metamaterials are unavailable and metals have their plasma frequency. Our results pave the way for a cost-effective platform enabling efficient steering of radiation angular momentum at the nanoscale.

A. C. and C. R. acknowledge support from U.S. Army International Technology Center Atlantic for financial support (Grant No. W911NF-14-1-0315).

- 
- [1] L. Marrucci, E. Karimi, S. Slussarenko, B. Piccirillo, E. Santamato, E. Nagali, and F. Sciarrino, *J. Opt.* **13**, 064001 (2011).
- [2] K. Y. Bliokh, F. J. Rodriguez-Fortuno, F. Nori, and A. V. Zayats, *Nat. Photonics* **9**, 796 (2015).
- [3] Y. Zhao, J. S. Edgar, G. D. M. Jeffries, D. McGloin, and D. T. Chiu, *Phys. Rev. Lett.* **99**, 073901 (2007).
- [4] K. Y. Bliokh, E. A. Ostrovskaya, M. A. Alonso, O. G. Rodriguez-Herrera, D. Lara, and C. Dainty, *Opt. Express* **19**, 26132 (2011).
- [5] A. Ciattoni, G. Cincotti, and C. Palma, *J. Opt. Soc. Am. A* **20**, 163 (2003).
- [6] E. Brasselet, Y. Izdebskaya, V. Shvedov, A. S. Desyatnikov, W. Krolikowski, and Y. S. Kivshar, *Opt. Lett.* **34**, 1021 (2009).
- [7] L. Marrucci, C. Manzo, and D. Paparo, *Phys. Rev. Lett.* **96**, 163905 (2006).
- [8] F. Manni, K. G. Lagoudakis, T. K. Paräiso, R. Cerna, Y. Léger, T. C. H. Liew, I. A. Shelykh, A. V. Kavokin, F. Morier-Genoud, and B. Deveaud-Plédran, *Phys. Rev. B* **83**, 241307(R) (2011).
- [9] N. A. Khilo, E. S. Petrova, and A. A. Ryzhevich, *Quantum Electron.* **31**, 85 (2001).
- [10] M. Yavorsky and E. Brasselet, *Opt. Lett.* **37**, 3810 (2012).
- [11] K. T. Gahagan and G. A. Swartzlander, *Opt. Lett.* **21**, 827 (1996).
- [12] G. Gbur and R. K. Tyson, *Josa A* **25**, 225 (2008).
- [13] Z. X. Wang, N. Zhang, and X. C. Yuan, *Opt. Express* **19**, 482 (2011).
- [14] N. Shitrit, I. Yulevich, E. Maguid, D. Ozeri, D. Veksler, V. Kleiner, and E. Hasman, *Science* **340**, 724 (2013).
- [15] G. Li, M. Kang, S. Chen, S. Zhang, E. Y. -B. Pun, K. W. Cheah, and J. Li, *Nano Lett.* **13**, 4148 (2013).
- [16] D. Hakobyan, H. Magallanes, G. Seniutinas, S. Juodkazis, and E. Brasselet, *Adv. Opt. Mater.* **4**, 306 (2016).
- [17] Y. Yang, W. Wang, P. Moitra, I. I. Kravchenko, D. P. Briggs, and J. Valentine, *Nano Lett.* **14**, 1394 (2014).
- [18] S. Chen, Y. Cai, G. Li, S. Zhang, and K. W. Cheah, *Laser Photonics Rev.* **10**, 322 (2016).
- [19] M. Silveirinha and N. Engheta, *Phys. Rev. Lett.* **97**, 157403 (2006).
- [20] A. Alú, M. G. Silveirinha, A. Salandrino, and N. Engheta, *Phys. Rev. B* **75**, 155410 (2007).
- [21] A. Ciattoni, C. Rizza, and E. Palange, *Phys. Rev. A* **81**, 043839 (2010).
- [22] C. Argyropoulos, P. Y. Chen, G. DAguanno, N. Engheta, and A. Alú, *Phys. Rev. B* **85**, 045129 (2012).
- [23] A. Ciattoni, C. Rizza, A. Marini, A. Di Falco, D. Faccio, and M. Scalora, *Laser Photonics Rev.* **10**, 517 (2016).
- [24] M. Z. Alam, I. De Leon, and R. W. Boyd, *Science* **352**, 795 (2016).
- [25] A. Ciattoni, A. Marini, and C. Rizza, *Opt. Lett.* **41**, 3102 (2016).
- [26] W. Zhu and W. She, *Opt. Lett.* **40**, 2961 (2015).
- [27] See Supplemental Material at <http://link.aps.org/supplemental/10.1103/PhysRevLett.118.104301> for the detailed evaluation of the vortex generation efficiency.
- [28] F. Forstmann and R. R. Gerhardt, *Metal Optics Near the Plasma Frequency* (Springer-Verlag, New York, 1986).
- [29] G. V. Naik, J. Kim, and A. Boltasseva, *Opt. Mater. Express* **1**, 1090 (2011).
- [30] A. Capretti, Y. Wang, N. Engheta, and L. Dal Negro, *ACS Photonics* **2**, 1584 (2015).